


Multichannel Topological Transport in an Acoustic Valley Hall Insulator

Zhenyu Wang,¹ Yuzhen Yang,² Houyin Li,¹ Han Jia,² Jinlong Luo,¹ Jian Huang,¹ Zhennan Wang,¹
Bo Jiang,¹ Ningjing Yang,¹ Guojun Jin,^{1,3,*} and Hai Yang^{1,†}

¹*School of Physics Science and Technology, Kunming University, Kunming, 650214, China*

²*Key Laboratory of Noise and Vibration Research, Institute of Acoustics, Chinese Academy of Sciences, 100190 Beijing, People's Republic of China*

³*National Laboratory of Solid State Microstructures, Department of Physics, and Collaborative Innovation Center of Advanced Microstructures, Nanjing University, Nanjing, 210093, China*

 (Received 20 October 2020; revised 27 December 2020; accepted 8 January 2021; published 8 February 2021)

Valley interface states, resulting in acoustic valley Hall topological insulators, have recently become a hot topic in the study of acoustic systems. On the basis of structural diversity and potential applications, we construct a two-dimensional triangular-lattice phononic crystal with C_{3v} -symmetric scatterers, and obtain two distinct valley Hall phases with nonvanishing valley Chern indices by rotating the scatterers. We numerically calculate the dispersion relations of these valley Hall phases including two kinds of interfaces, and find that valley interface states exist at not only the zigzag interface but also the armchair interface. We demonstrate the acoustic splitting and merging of valley interface states in the cross-waveguides, and numerically achieve the XOR and OR logic functions. We also design three complicated waveguides by assembling phononic crystals with distinct valley Hall phases. By experimental measurements in these waveguides, we successfully implement one-, two-, and three-channel topological transport. This research possibly provides a design route exploiting valley interface states to fabricate multichannel acoustic communication devices.

DOI: [10.1103/PhysRevApplied.15.024019](https://doi.org/10.1103/PhysRevApplied.15.024019)

I. INTRODUCTION

Topological insulators possess insulating states in the bulk and conducting states on the interface, and have potential applications in electronic communications [1]. Researchers have studied the exotic properties of topological insulators, including one-way transmission without backscattering and defect-insensitive transport. In recent years, this hot field has been extended to optical systems [2] and acoustic systems [3,4]. Investigations on two-dimensional (2D) acoustic topological insulators have made considerable progress, and there are three principal mechanisms. Firstly, acoustic quantum Hall insulators are constructed by introducing circulating fluids to simulate an effective magnetic field [5–8], and chiral topological edge states are realized when the time-reversal symmetry is broken. Secondly, acoustic quantum spin Hall insulators are formed without breaking the time-reversal symmetry, mainly by simulating the pseudo-spin states, through contracting and expanding the metamolecules [9–13], or rotating scatterers [14–16], to control the topological properties of the band structure of phononic

crystals (PCs). On the other hand, the active control method provides a convenient way for tuning the wave properties, such as by use of negative-capacitance circuits [17]. Thirdly, acoustic valley Hall topological insulators are achieved by breaking the space-inversion symmetry [18,19] but maintaining the time-reversal symmetry.

Because of its flexibility and diversity, acoustic valley physics has become a rapidly developing research field. Hence, many acoustic valley Hall topological insulators have been proposed, including fluid-borne systems [20–36] and elastic wave systems [37–50]. In these acoustic valley materials, there are two kinds of valley states with different properties. One is the valley bulk state with vortex chirality, which is used to split the acoustic waves from different valleys [18,20,22,31] and to manipulate particles without contact [29]. The other state is the valley interface state with the backscattering immunity and defect insensitivity, which can give one-way and robust acoustic transmissions. Besides, this valley interface state can be used to realize many fascinating phenomena, such as an interlayer converter [21], acoustic partition [26,27,31,34,48,49], and negative refraction [23,31]. Recently, some studies extended the valley states in acoustic topological metamaterials to more-complex systems [25,28,36]; however, the relative traditionally topological phenomena still need to

*gjin@nju.edu.cn

†kmyangh@263.net

be explored further. For example, can we obtain a controllable logic gate in acoustic valley materials? Can we design some feasible waveguides to get multichannel transmission? We resolve these two questions in the following.

In this work, we design a 2D triangular-lattice PC constructed from C_{3v} -symmetric scatterers, and its space-inversion symmetry can be broken by rotating them. We obtain the valley bulk states with vortex chirality. For two distinct valley Hall phases with nonzero valley Chern numbers, the topological phase transition can occur if the rotational angle is changed. Next we construct two kinds of heterostructures with a zigzag interface or an armchair interface, and find that their dispersion relations are very distinct. We observe that one of the modes for the zigzag interfaces is hardly excited, but the other modes are robust with regard to crystal defects. Furthermore, we implement acoustic splitting and merging of valley interface states in a cross-waveguide, and obtain two controllable logic gates. Finally, we numerically and experimentally demonstrate that one-, two-, and three-channel acoustic valley transport is feasible in the complicated waveguides, which may open a route toward multichannel-communication applications based on acoustic splitting and merging of valley interface states. In our work, the simulations are performed with the finite-element commercial software program COMSOL MULTIPHYSICS.

The remainder of this paper is organized as follows. In Sec. II, we construct a 2D PC and its variants with scatterers, calculate their band structures, and give the phase diagram. In Sec. III, we explore and analyze the valley interface states at the zigzag and armchair interfaces. On the basis of these two kinds of interfaces, we fabricate cross-waveguides and discuss the acoustic splitting and merging in Sec. IV. Experimental verification of multichannel transport is presented in Sec. V. Finally, in Sec. VI, the main conclusions are given regarding the whole work.

II. STRUCTURE BUILDING, ENERGY BAND, AND PHASE DIAGRAM

As shown in Fig. 1(a), a 2D PC is constructed by our arranging a triangular-lattice array of scatterers in an air medium [32,51]. Each scatterer is a hollow cylinder with three equal splits, and the included angle is 120° between any two adjacent splits. We choose a photosensitive resin to fabricate the scatterers (gray region), which are regarded as a rigid body compared with the air background (white region). In this airborne system, the mass density and the wave velocity of air are 1.21 kg/m^3 and 343 m/s , respectively. In a unit cell, the lattice constant $a = 2.0 \text{ cm}$, the width of each split $d = 0.1 \text{ cm}$, and the inner radius r_1 and outer radius r_2 of every hollow cylinder are 0.38 and

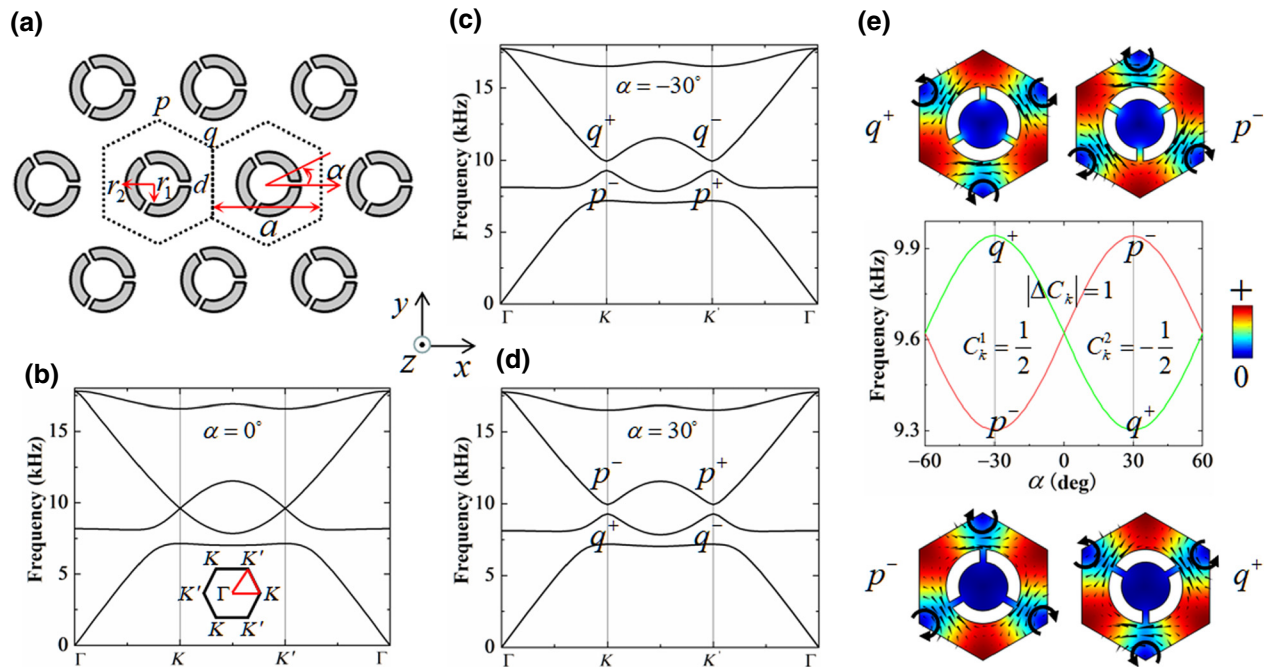


FIG. 1. (a) A 2D triangular-lattice PC made of photosensitive resin (gray region) immersed in an air background (white region). The hexagons with dotted black lines are two unit cells. The p and q points are two representative points satisfying C_3 symmetry in a unit cell. (b) Band structure of the PC with $\alpha = 0^\circ$. The inset shows the first Brillouin zone. (c),(d) Band structures of the PC with $\alpha = -30^\circ$ and $\alpha = 30^\circ$, respectively. p^- and q^+ (p^+ and q^-) are the valley bulk states at the K (K') point. (e) The middle panel displays a phase diagram that shows a topological phase transition when α changes from -60° to 60° at the K point. The top and bottom panels are the absolute-pressure-field distributions of the valley bulk states corresponding to $\alpha = -30^\circ$ and $\alpha = 30^\circ$ (vertical solid gray lines in the middle panel). The black arrows represent the energy flux of acoustic waves.

0.58 cm, respectively. To break the space-inversion symmetry, all the scatterers in the PC are rotated around their respective centers of the unit cells. A rotation is denoted by the angle α relative to the x axis. It is assumed that the counterclockwise (clockwise) rotation corresponds to $\alpha > 0$ ($\alpha < 0$). Besides, the p and q points are the positions with C_3 symmetry in the unit cell, which are used to characterize the properties of valley bulk states.

Scatterers with C_{3v} symmetry in a 2D triangular-lattice PC inevitably produce Dirac degeneracy in the first Brillouin zone [52]. In Fig. 1(b), the twofold Dirac degeneracies emerge at the points K and K' when $\alpha = 0$. This deterministic degeneracy originates from the rotational symmetry of scatterers in their unit cell. Thus we need to break the symmetry in order to lift the Dirac degeneracy. As shown in Figs. 1(c) and 1(d), the Dirac degeneracies at the points K and K' are lifted to open the omnidirectional band gaps by rotating the scatters in a clockwise ($\alpha = -30^\circ$) or counterclockwise ($\alpha = 30^\circ$) direction. Here, we see two valleys (i.e., valleys K and K'), and each valley possesses two separated valley bulk states. Because of the time-reversal symmetry of the 2D PC, the two valleys have opposite chirality, so we need to consider only one of the valleys (e.g., the K valley). In Fig. 1(c), for $\alpha = -30^\circ$, the lower and upper valley bulk states have clockwise ($-$) and counterclockwise ($+$) energy-flow vortices, which are noted as p^- and q^+ , respectively. In contrast, the lower and upper valley bulk states for $\alpha = 30^\circ$ in Fig. 1(d) are q^+ and p^- , respectively. Obviously, a band-inversion process occurs between $\alpha = -30^\circ$ and $\alpha = 30^\circ$. Besides, we observe the appearance of flat bands in the first and second bands from Figs. 1(b)–1(d), corresponding to zero group velocity and showing the high spatial localization, which originate from the three-split hollow cylinders acting like acoustic resonators.

To show the topological property of the band structure of the 2D PC, we study the evolution of valley bulk states at the K valley when the rotation angle α changes from -60° to 60° . As shown in Fig. 1(e), when $\alpha = n\pi/3$ ($n = -1, 0, 1$), the Dirac degeneracy is protected due to the C_{3v} symmetry. However, when $\alpha \neq n\pi/3$, the Dirac degeneracy is lifted to form a band gap since the C_{3v} symmetry reduces to C_3 symmetry. From the top and bottom panels in Fig. 1(e), we observe the vortex chirality of acoustic energy flow, which can be called “pseudospin.” For $-60^\circ < \alpha < 0^\circ$, the lower and upper valley bulk states are the vortices of clockwise (p^-) and counterclockwise (q^+) directions, respectively. In contrast with $-60^\circ < \alpha < 0^\circ$, the vortices of lower and upper valley bulk states for $0^\circ < \alpha < 60^\circ$ are counterclockwise (q^+) and clockwise (p^-), respectively. Hence, the topological phase transition occurs from $\alpha < 0$ to $\alpha > 0$. Considering the $\mathbf{k} \cdot \mathbf{p}$ perturbation method around the K valley, we obtain the sign of the effective mass m from an extracted term of the α -related continuum Hamiltonian $H_K(\delta\mathbf{k}) = v_D\delta k_x\sigma_x + v_D\delta k_y\sigma_y +$

$mv_D^2\sigma_z$ [19]. This term produces a nontrivial Berry curvature $\Omega_k(\delta\mathbf{k}) = mv_D/2(\delta\mathbf{k}^2 + m^2v_D^2)^{3/2}$, and hence the Berry phase γ_k can be defined as the integral of the Berry curvature in the first Brillouin zone; that is, $\gamma_k = \int \Omega_k(\delta\mathbf{k})ds$. The acoustic valley Chern numbers C_K have 2π phase difference compared with γ_k , and hence can be written as [19,27,30,32]

$$C_K = \frac{\gamma_k}{2\pi} = \frac{1}{2}\text{sgn}[m] = \frac{1}{2}\text{sgn}\left(\frac{\pi(f_+ - f_-)}{v_D^2}\right), \quad (1)$$

where f_+ and f_- are the frequencies of the valley bulk states corresponding to the counterclockwise and clockwise energy-flow vortices, respectively, and v_D is the Dirac velocity. From Eq. (1), $C_K^1 = 1/2$ for $\alpha < 0$, but $C_K^2 = -1/2$ for $\alpha > 0$, and then $|\Delta C_K| = |C_K^2 - C_K^1| = 1$. So the topological invariant is nonzero between the two distinct valley Hall phases, which indicates that acoustic valley interface states must exist at the interface of the PCs composed of the two distinct valley Hall phases.

III. VALLEY INTERFACE STATES AT ZIGZAG AND ARMCHAIR INTERFACES

After knowing that there are two distinct valley Hall phases, we can assemble them to form two heterostructures with different interfaces. Generally, there are two kinds of interfaces in a 2D triangular-lattice PC: a zigzag interface and an armchair interface. We choose two configurations (i.e., $\alpha = -30^\circ$ and $\alpha = 30^\circ$) to design two heterostructures. Firstly, we construct an $a \times 14\sqrt{3}a$ heterostructure with zigzag interfaces (the size is noted as the length in the x direction times the length in the y direction). Here, a PC plate with $\alpha = -30^\circ$ is sandwiched between two PC plates with $\alpha = 30^\circ$ along the y axis, as shown in Fig. 2(a). The interface between the top PC plate with $\alpha = 30^\circ$ and the middle PC plate with $\alpha = -30^\circ$ is labeled as I1, and I2 refers to the interface between the middle PC plate with $\alpha = -30^\circ$ and the bottom PC plate with $\alpha = 30^\circ$. Secondly, a $44a \times \sqrt{3}a$ heterostructure with armchair interfaces is designed by our arranging a PC plate with $\alpha = -30^\circ$ in the middle of two PC plates with $\alpha = 30^\circ$ along the x axis, as shown in Fig. 2(d). Similarly, the interface between the left PC plate with $\alpha = 30^\circ$ and the middle PC plate with $\alpha = -30^\circ$ is labeled as I3, and I4 is the interface between the middle PC plate with $\alpha = -30^\circ$ and the right PC plate with $\alpha = 30^\circ$. Finally, we apply periodic boundary conditions on the left and right boundaries of the heterostructure with zigzag interfaces I1 and I2. However, for the heterostructure with the armchair interfaces I3 and I4, the periodic boundary conditions are imposed on the upper and lower boundaries.

The dispersion relations of the two heterostructures with zigzag or armchair interfaces are plotted in Figs. 2(b) and 2(e), respectively. The bulk bands are represented by the

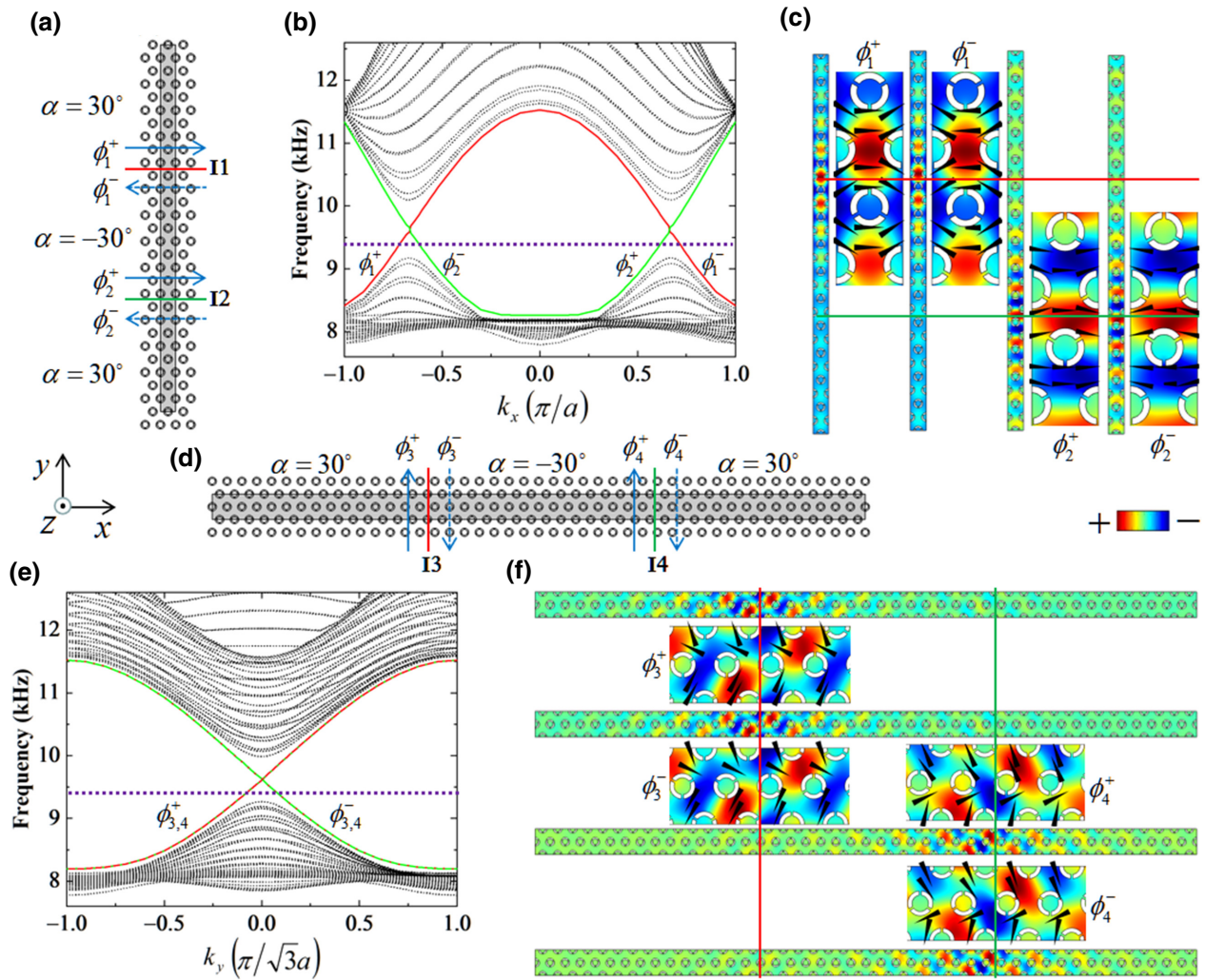


FIG. 2. (a) $a \times 14\sqrt{3}a$ heterostructure with zigzag interfaces. Interfaces I1 and I2 are represented by the horizontal solid red and green lines, respectively, and they have forward (ϕ_1^+ and ϕ_2^+) and backward (ϕ_1^- and ϕ_2^-) interface modes. (b) Dispersion relation corresponding to the heterostructure in (a). The heterostructure with lattice constant a in the x direction, and corresponding reciprocal lattice vector $2\pi/a$. The dotted black lines are the bulk bands, and the solid red and green lines represent the valley interface states of I1 and I2, respectively. (c) Total-pressure-field distributions of the four valley interface states at the same frequency [horizontal dotted purple line in (b)]. The four insets show enlarged views of I1 and I2, and the black arrows represent the energy flux of acoustic waves. (d) $44a \times \sqrt{3}a$ heterostructure with armchair interfaces. Interfaces I3 (vertical solid red line) and I4 (vertical solid green line) have the upward (ϕ_3^+ and ϕ_4^+) and downward (ϕ_3^- and ϕ_4^-) interface modes. (e) Dispersion relation corresponding to the heterostructure in (d). The heterostructure with lattice constant $\sqrt{3}a$ in the y direction, and corresponding reciprocal lattice vector $2\pi/(\sqrt{3}a)$. The solid (dotted) red and green lines represent the valley interface states of I3 and I4, respectively. (f) Total-pressure-field distributions of the four valley interface states at the same frequency [horizontal dotted purple line in (e)]. The four insets show enlarged views of I3 and I4.

dotted black lines. For the heterostructure with zigzag interfaces, the valley interface states of I1 (solid red line) and I2 (solid green line) emerge in the energy gaps. By our choosing the same frequency (dotted purple line), the total-pressure-field distributions of the four valley interface states are illustrated in Fig. 2(c), and these interface states are tightly confined around the interfaces. According to the directions of the group velocities, the four valley interface states are divided into the forward modes (ϕ_1^+ and

ϕ_2^+) and backward modes (ϕ_1^- and ϕ_2^-), which are in accord with the energy-flow directions (black arrows) shown in the insets in Fig. 2(c). Similarly, the valley interface states of the heterostructure with armchair interfaces I3 and I4 are depicted in Fig. 2(e), and are labeled as ϕ_3^+ (solid red line), ϕ_4^+ (dotted green line), ϕ_3^- (dotted red line), and ϕ_4^- (solid green line), respectively. From the insets in Fig. 2(f), the positive and negative group velocities correspond to the upward modes (ϕ_3^+ and ϕ_4^+) and downward modes (ϕ_3^-

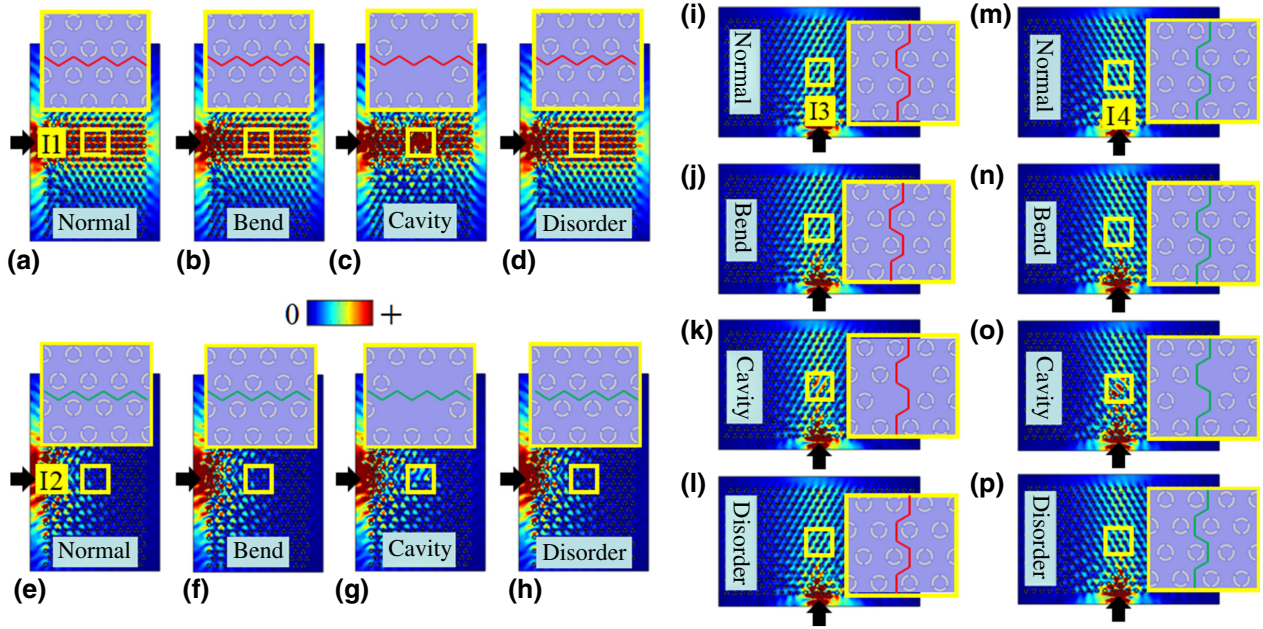


FIG. 3. Robust sound transport for valley interface states at 9300 Hz: (a)–(h) zigzag interfaces and (i)–(p) armchair interfaces. (a) Excitation of ϕ_1^+ for the normal interface. (b)–(d) Excitation of ϕ_1^+ for the interfaces with a bend, a cavity, and disorder, respectively. The excitations for the other valley interface modes are shown in a similar fashion. (e)–(h), (i)–(l), (m)–(p) Excitations of ϕ_2^+ , ϕ_3^+ , and ϕ_4^+ , respectively. The narrow Gaussian beams are represented by the black arrows. The regions surrounded by the yellow boxes represent the positions of crystal defects, and their enlarged views are shown in the corresponding insets.

and ϕ_4^-), respectively. The valley interface states for the heterostructure with armchair interfaces (e.g., ϕ_3^+) exist in the entire momentum space; however, those for the heterostructure with zigzag interfaces (e.g., ϕ_1^+) exist only in a half of momentum space. Namely, the valley interface states for the heterostructure with zigzag interfaces are pure valley states (K or K'), whereas those for the heterostructure with armchair interfaces are mixed valley states (K and K'). Moreover, it is worth noting that the valley interface states with the same propagation directions for the heterostructure with armchair interfaces are always degenerate (fourfold degeneracy exists at $k_y = 0$) in the entire momentum space, such as ϕ_3^+ and ϕ_4^+ and ϕ_3^- and ϕ_4^- , which are different from the valley interface states of the heterostructure with zigzag interfaces.

As shown in Fig. 3, we design four samples composed of two PCs with different rotation angles $\alpha = 30^\circ$ and -30° , which possess the interfaces I1, I2, I3, and I4, respectively. Each sample consists of two domains, and each domain includes 12 scatterers in the x direction and 16 scatterers in y direction, and thus there are 12×16 scatterers. To excite the four valley interface states ϕ_1^+ , ϕ_2^+ , ϕ_3^+ , and ϕ_4^+ , we apply the same narrow Gaussian beams on the left and bottom sides of the samples, as shown by the black arrows in Fig. 3. The three valley interface states (absolute-pressure-field distributions) are excited [i.e., ϕ_1^+ in Fig. 3(a), ϕ_3^+ in Fig. 3(i), and ϕ_4^+ in Fig. 3(m)]; however, the valley interface state ϕ_2^+ in Fig. 3(e) with the

antisymmetric interface mode, as shown in the inset in Fig. 2(c), cannot be excited at the same frequency, which is consistent with the previous results [19,26]. In addition, the excited ϕ_3^+ and ϕ_4^+ are weaker than the excited ϕ_1^+ , and they have tilted propagation modes [51], which differs from the straight propagation mode of the excited ϕ_1^+ . The tilted propagation modes indicate that the corresponding excitations with a certain angle are more efficient than that in Figs. 3(i)–3(p), as demonstrated in Ref. [26]. Furthermore, we also show the robustness of these valley interface states by introducing three types of defects (i.e., bend, cavity, and disorder) on these interfaces, which are sketched in Figs. 3(b)–3(d), 3(f)–3(h), 3(j)–3(l), and 3(n)–3(p). If we excite the four valley interface states for the opposite modes (i.e., ϕ_1^- , ϕ_2^- , ϕ_3^- , and ϕ_4^-), the results are similar to the case of ϕ_1^+ , ϕ_2^+ , ϕ_3^+ , and ϕ_4^+ .

IV. ACOUSTIC SPLITTING AND MERGING OF VALLEY INTERFACE STATES

The fascinating splitting phenomena of valley interface states were recently demonstrated in acoustic and elastic wave systems [26,27,31,34,48,49]. Here, in cross-waveguides, we not only implement acoustic splitting but also realize acoustic merging. The samples are rectangles, separated into four domains, as shown in Figs. 4(a) and 4(b). The top-left and bottom-right domains correspond to the configuration $\alpha = 30^\circ$, and the bottom-left

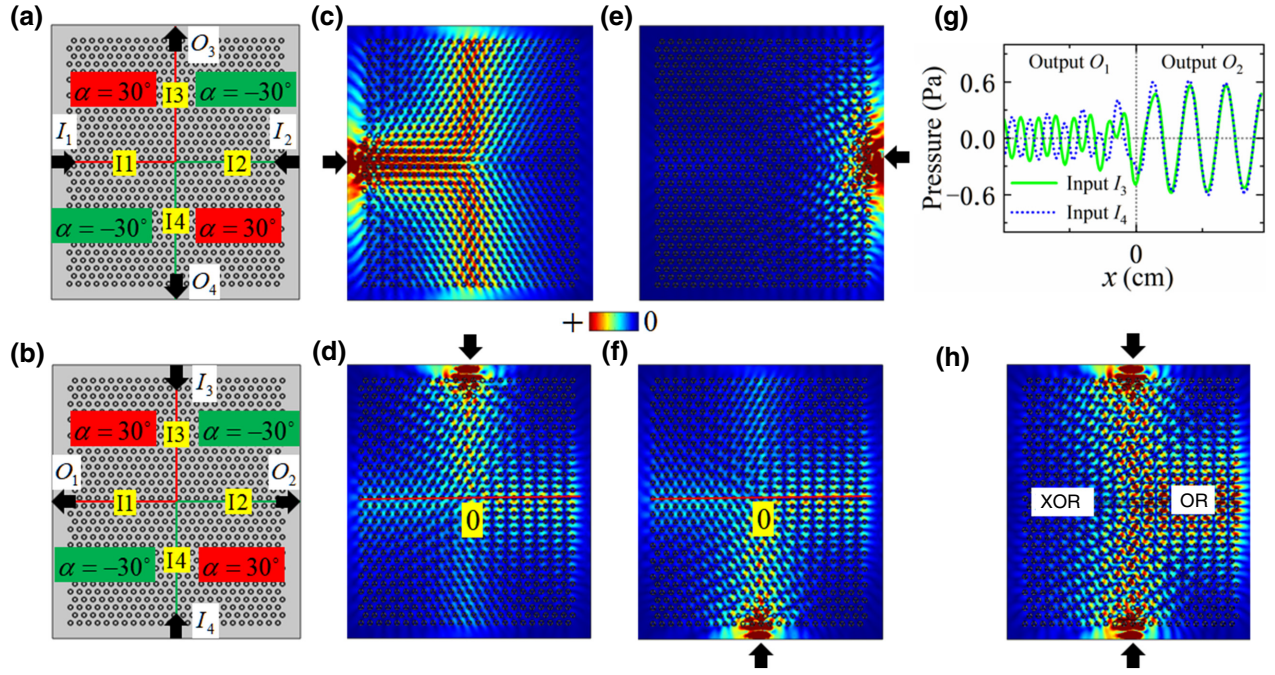


FIG. 4. Acoustic splitting and merging of valley interface states and logic functions at a frequency of 9300 Hz. (a),(b) Cross-waveguide samples composed of two distinct valley Hall phases. The rectangular sample is divided into four domains by the horizontal (I1 and I2) and vertical (I3 and I4) interfaces, and each domain is composed of 12×16 scatterers. I_1 – I_4 and O_1 – O_4 are the input and output ports, respectively. (c)–(f) Absolute-pressure-field distributions for the narrow Gaussian beams (black arrows) launched from I_1 , I_3 , I_2 , and I_4 , respectively. Acoustic splitting emerges in (c),(d),(f). (g) Distributions of acoustic pressure field in (d),(f) along the horizontal interfaces. (h) Acoustic merging as there are incident waves from both input ports I_3 and I_4 , which realizes the XOR and OR logic functions.

and top-right domains correspond to the configuration $\alpha = -30^\circ$. In Fig. 4(a), the input and output ports (I_1 and I_2 and O_3 and O_4) are horizontal and vertical, respectively, and the cases (I_3 and I_4 and O_1 and O_2) in Fig. 4(b) are reversed. In simulations, we use the same narrow Gaussian beams (black arrows) to excite the valley interface states. As shown in Fig. 4(c), acoustic splitting of the valley interface state is observed when the input port is I_1 . The valley interface state in I1 is excited and arrives at the center of sample, and bisects equally into I3 and I4 owing to the structural symmetry instead of going straight into I2. The excited valley interface state in I1 (ϕ_1^+) is from the K' valley, which couples with those in I3 (ϕ_3^+) and I4 (ϕ_4^-), which can be regarded as mixed valley states; however, it cannot couple with that in I2 (ϕ_2^+) from the K valley. Besides, the valley interface state of I2 cannot be excited as the input port is I_2 , as shown in Fig. 4(e).

If the input port is I_3 or I_4 , we observe abnormal splitting of valley interface states. Since I3 and I4 are symmetric in the sample, similar results are obtained. As shown in Figs. 4(d) and 4(f), the excited valley interface states go into the three interfaces at the intersection. It is worth noting that the valley interface state of I2 is excited. Besides, the transport for the valley interface state into I2 is greatly enhanced, and transport into I1 is weaker than that into I2.

Most interestingly, the transport into I4 [Fig. 4(d)] or I3 [Fig. 4(f)] exists unexpectedly, although it is greatly suppressed, which originates from the valley mixed state of I3 or I4. In previous work, the acoustic abnormal splitting phenomena of valley interface states in a cross-waveguide depend only on the tilted interface, which leads to the spatial overlap of the valley interface modes [31,41]; however we can achieve the abnormal splitting phenomena in cross-waveguides with orthogonal interfaces. In addition, for the abnormal splitting phenomena in Figs. 4(d) and 4(f), we find that the acoustic pressure distributions of the output ports O_1 and O_2 are out of phase and in phase, respectively, and have nearly the same amplitudes, as sketched in Fig. 4(g). Thus the acoustic merging of valley interface states can be realized in Fig. 4(h) when the input ports are I_3 and I_4 .

As depicted in Fig. 4(h), ignoring the excited valley interface states of the input ports in Figs. 4(d) and 4(f), we find that the output ports O_1 and O_2 possess the XOR and OR logic functions, respectively. Here, if the valley interface states are excited in the two input ports I_3 and I_4 , this is noted as “1,” otherwise “0.” Hence, for Figs. 4(d), 4(f), and 4(h), the input states $\{I_3, I_4\}$ are $\{1, 0\}$, $\{0, 1\}$, and $\{1, 1\}$, respectively. For input states $\{1, 0\}$ and $\{0, 1\}$, the similar results show that the valley interface states of output ports

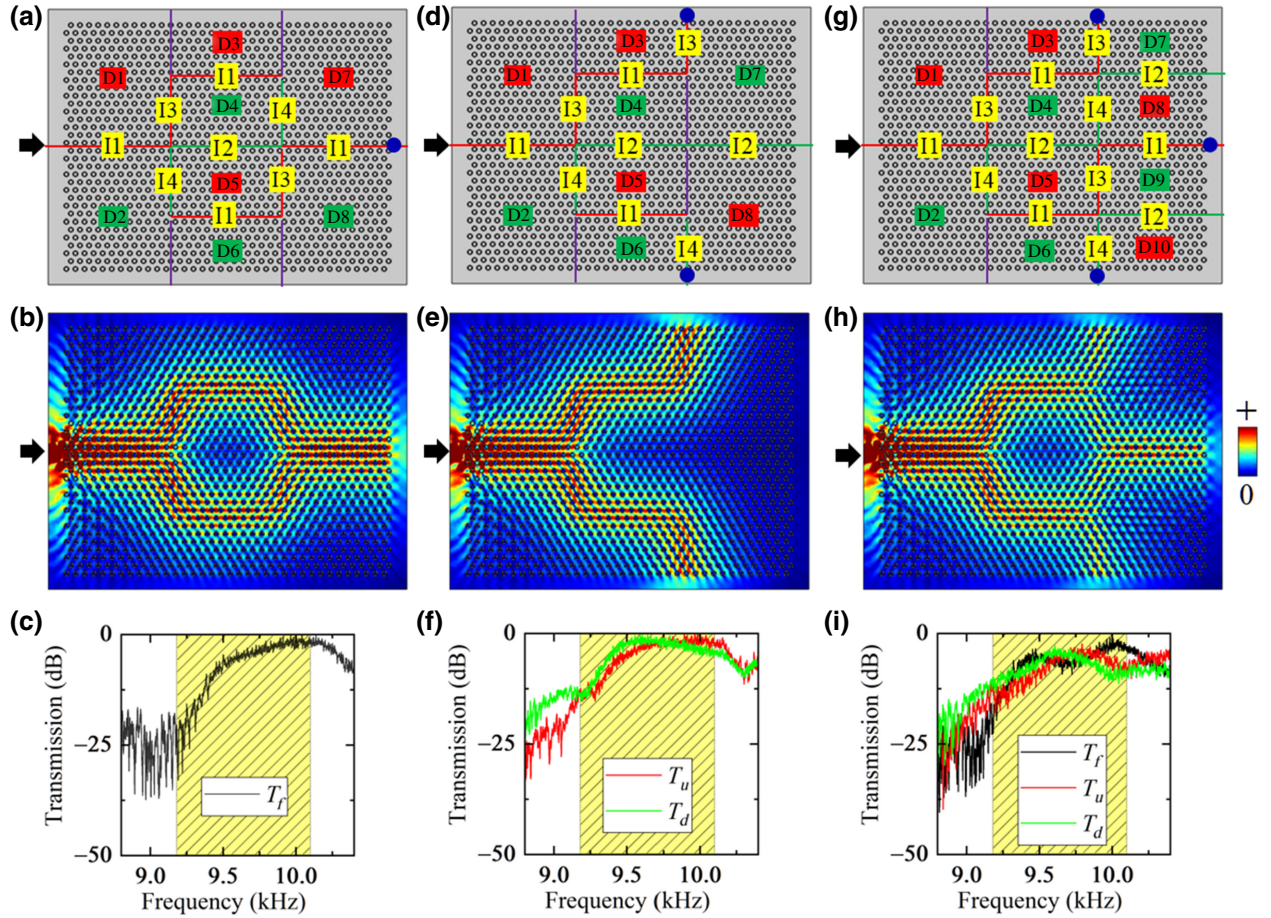


FIG. 5. Multichannel transport of the valley interface states. (a),(d),(g) Complicated waveguides composed of two phases for one-, two-, and three-channel valley topological transport, respectively. The different interfaces and phases are marked on these samples. The black arrows and solid blue circles represent the acoustic sources and detectors, respectively. (b),(e),(h) Simulated pressure-field distributions at a frequency of 9300 Hz for one-, two-, and three-channel valley topological transport, respectively. (c),(f),(i) Measured transmission spectra for the cases in (a),(d),(g), respectively. The topological band gaps are represented by the yellow regions. T_f , T_u , and T_d are the forward (solid black lines), upward (solid red lines), and downward (solid green lines) valley topological transport, respectively.

O_1 and O_2 are both excited. However, only the valley interface state of output port O_2 is excited as the input state is $\{1, 1\}$. Hence, the output states $\{O_1, O_2\}$ can be regarded as $\{1, 1\}$, $\{1, 1\}$, and $\{0, 1\}$. Then, for the output ports O_1 and O_2 , we realize the XOR and OR logic functions, respectively. Besides, if we exchange the positions of distinct valley Hall phases, the logic functions are opposite those in Fig. 4(h). Compared with the results reported in the acoustic quantum spin Hall insulator [13], our acoustic valley Hall system does not need a programmable coding process, and therefore it is easier to implement for controllable logic gates.

V. EXPERIMENTAL VERIFICATION OF MULTICHANNEL TRANSPORT

Recently, a four-port topological acoustic switch was realized by means of acoustic valley material [36], which

shows some interesting acoustic transmission phenomena in simple waveguides. Here, compared with Ref. [36], we implement richer physical phenomena and more applications. On the basis of the above results, we can combine the acoustic splitting and merging phenomena to achieve multichannel transport of valley interface states in complicated waveguides. In experiments, the scatterers are fabricated by three-dimensional printing, and are arranged in a triangular-lattice array to form the samples, which are sandwiched by upper and lower rigid plates. The scatterers and the plates are both made of photosensitive resin, and the heights of scatterers are 1 cm. As shown in Figs. 5(a), 5(d), and 5(g), we design three rectangular samples (sizes $0.87 \times 0.697 \text{ m}^2$) with different interfaces, which correspond to complicated waveguides with one, two, and three output channels, respectively. In Fig. 5(a), the one-channel-transport waveguide consists of eight domains (D1–D8), the configurations with $\alpha = 30^\circ$ correspond to

domains D1 and D7 (12×16 scatterers) and domains D3 and D5 (12×8 scatterers), and the configurations with $\alpha = -30^\circ$ correspond to domains D2 and D8 (12×16 scatterers) and domains D4 and D6 (12×8 scatterers). The two-channel-transport waveguide is constructed on the basis of the one-channel-transport waveguide by our exchanging only the positions of domains D7 and D8, as shown in Fig. 5(d). For the three-channel-transport waveguide in Fig. 5(g), only domains D7 and D8 are divided into four domains with 12×8 scatterers [i.e., domains D7 and D9 ($\alpha = -30^\circ$) and domains D8 and D10 ($\alpha = 30^\circ$)] compared with the one-channel-transport waveguide. In experiments, acoustic sources (speakers, black arrows) at the input ports of the samples are used to excite the valley interface states, and detectors (microphones, solid blue circles) at the output ports of the samples are used to obtain the measured transmissions.

In Figs. 5(b), 5(e), and 5(h), we display the absolute-pressure-field distributions from simulations at 9300 Hz for the three complicated waveguides. The transmission spectra (8800–10 400 Hz) in experiments are sketched in Figs. 5(c), 5(f), and 5(i), and the topological band gap (9180–10 100 Hz) is shown by the yellow regions. First, for one-channel valley topological transport, the transport for the valley interface state into I1 diverges equally at the first intersection, into I3 and I4, and does not enter straight into I2. Subsequently, the transports into I3 and I4 both go through the two connected I1s, and go into I4 and I3, respectively, and converge at the second intersection. Ultimately, the transport passes I1. In short, the acoustic waves successfully pass through complicated routes from the left input port to the right output port. Moreover, the two-channel valley topological transport is equally separated into two transports at the first intersection. One is the upward transport, and passes I3, I1, and I3 in proper order; however, another transport is the downward transport, and goes through I4, I1, and I4 in proper sequence. In the two-channel transport, the acoustic waves launched from the left input port can be transmitted to the top and bottom output ports, and the two transports are equal due to the structural symmetry, as shown in Fig. 5(f). Finally, three-channel transport is more complicated than one-channel transport and two-channel transport, and the corresponding valley topological transport can be divided into three transports (i.e., forward, upward, and downward transports). The upward and downward transports are equal, and they compete with the forward transport. In other words, the forward transport is suppressed when the upward and downward transports are dominant, and vice versa. The upward and downward transports are stronger than the forward transport when the frequency range in the topological band gap is from 9500 to 9750 Hz, as shown in Fig. 5(i). For three-channel transport, the acoustic waves can be transferred from the left input port to the top, bottom, and right output ports, and the three outgoing transports

are equal as long as the valley interface state frequencies are proper, such as 9500 and 9750 Hz. These results can help to construct multichannel acoustic valley topological transport devices by using complicated waveguides with different interfaces.

VI. CONCLUSIONS

In summary, we find that valley interface states occur at zigzag as well as armchair interfaces in heterostructures made of a 2D triangular-lattice PC with distinct valley Hall phases. The dispersion relations and propagation modes of the valley interface states are both distinct for the zigzag and armchair interfaces. By using different interfaces, we realize the acoustic splitting and merging phenomena of the valley interface states in cross-waveguides, and demonstrate that there are controllable logic gates in the acoustic merging. More importantly, multichannel acoustic topological transport of the valley interface states is demonstrated and verified by simulations and experiments. Our research provides an efficient way for exploring multichannel acoustic valley topological transport in complicated waveguides, which may be extended to other acoustic valley materials (e.g., underwater and elastic PCs). It is expected that our findings will contribute to the construction of multichannel acoustic communication devices based on valley topological insulators.

ACKNOWLEDGMENTS

This work was supported by the National Nature Science Foundation of China (Grants No. 11264022, No. 11874383, and No. 12074156) and Yunnan Local College Applied Basic Research Projects (Grant No. 2017FH001-001).

-
- [1] M. Z. Hasan and C. L. Kane, Topological insulators, *Rev. Mod. Phys.* **82**, 3045 (2010).
 - [2] T. Ozawa, H. M. Price, A. Amo, N. Goldman, M. Hafezi, L. Lu, M. C. Rechtsman, D. Schuster, J. Simon, O. Zilberberg, and I. Carusotto, Topological photonics, *Rev. Mod. Phys.* **91**, 015006 (2019).
 - [3] X. Zhang, M. Xiao, Y. Cheng, M.-H. Lu, and J. Christensen, Topological sound, *Commun. Phys.* **1**, 97 (2018).
 - [4] G. Ma, M. Xiao, and C. T. Chan, Topological phases in acoustic and mechanical systems, *Nat. Rev. Phys.* **1**, 281 (2019).
 - [5] A. B. Khanikaev, R. Fleury, S. H. Mousavi, and A. Alú, Topologically robust sound propagation in an angular-momentum-biased graphene-like resonator lattice, *Nat. Commun.* **6**, 8260 (2015).
 - [6] Z. Yang, F. Gao, X. Shi, X. Lin, Z. Gao, Y. Chong, and B. Zhang, Topological Acoustics, *Phys. Rev. Lett.* **114**, 114301 (2015).

- [7] Z.-G. Chen and Y. Wu, Tunable Topological Phononic Crystals, *Phys. Rev. Appl.* **5**, 054021 (2016).
- [8] A. Souslov, B. C. van Zuiden, D. Bartolo, and V. Vitelli, Topological sound in active-liquid metamaterials, *Nat. Phys.* **13**, 1091 (2017).
- [9] C. He, X. Ni, H. Ge, X.-C. Sun, Y.-B. Chen, M.-H. Lu, X.-P. Liu, and Y.-F. Chen, Acoustic topological insulator and robust one-way sound transport, *Nat. Phys.* **12**, 1124 (2016).
- [10] Z. Zhang, Q. Wei, Y. Cheng, T. Zhang, D. Wu, and X. Liu, Topological Creation of Acoustic Pseudospin Multipoles in a Flow-Free Symmetry-Broken Metamaterial Lattice, *Phys. Rev. Lett.* **118**, 084303 (2017).
- [11] Y. Deng, H. Ge, Y. Tian, M. Lu, and Y. Jing, Observation of zone folding induced acoustic topological insulators and the role of spin-mixing defects, *Phys. Rev. B* **96**, 184305 (2017).
- [12] Z. Zhang, Y. Tian, Y. Cheng, X. Liu, and J. Christensen, Experimental verification of acoustic pseudospin multipoles in a symmetry-broken snowflake-like topological insulator, *Phys. Rev. B* **96**, 241306(R) (2017).
- [13] J.-P. Xia, D. Jia, H.-X. Sun, S.-Q. Yuan, Y. Ge, Q.-R. Si, and X.-J. Liu, Programmable coding acoustic topological insulator, *Adv. Mater.* **30**, 1805002 (2018).
- [14] B.-Z. Xia, T.-T. Liu, G.-L. Huang, H.-Q. Dai, J.-R. Jiao, X.-G. Zang, D.-J. Yu, S.-J. Zheng, and J. Liu, Topological phononic insulator with robust pseudospin-dependent transport, *Phys. Rev. B* **96**, 094106 (2017).
- [15] M.-J. Tuo, L.-H. Zhang, D. Liu, R.-W. Peng, R.-H. Fan, Z.-G. Chen, Y. Wu, D.-X. Qi, and M. Wang, Twist-projected two-dimensional acoustic topological insulators, *Phys. Rev. B* **99**, 205432 (2019).
- [16] H. Huang, Z. Tan, S. Huo, L. Feng, J. Chen, and X. Han, Topologically protected zero refraction of elastic waves in pseudospin-hall phononic crystals, *Commun. Phys.* **3**, 46 (2020).
- [17] G.-H. Li, T.-X. Ma, Y.-Z. Wang, and Y.-S. Wang, Active control on topological immunity of elastic wave metamaterials, *Sci. Rep.* **10**, 9376 (2020).
- [18] J. Lu, C. Qiu, M. Ke, and Z. Liu, Valley Vortex States in Sonic Crystals, *Phys. Rev. Lett.* **116**, 093901 (2016).
- [19] J. Lu, C. Qiu, L. Ye, X. Fan, M. Ke, F. Zhang, and Z. Liu, Observation of topological valley transport of sound in sonic crystals, *Nat. Phys.* **13**, 369 (2017).
- [20] L. Ye, C. Qiu, J. Lu, X. Wen, Y. Shen, M. Ke, F. Zhang, and Z. Liu, Observation of acoustic valley vortex states and valley-chirality locked beam splitting, *Phys. Rev. B* **95**, 174106 (2017).
- [21] J. Lu, C. Qiu, W. Deng, X. Huang, F. Li, F. Zhang, S. Chen, and Z. Liu, Valley Topological Phases in Bilayer Sonic Crystals, *Phys. Rev. Lett.* **120**, 116802 (2018).
- [22] M. Wang, L. Ye, J. Christensen, and Z. Liu, Valley Physics in Non-Hermitian Artificial Acoustic Boron Nitride, *Phys. Rev. Lett.* **120**, 246601 (2018).
- [23] Z. Zhang, Y. Tian, Y. Wang, S. Gao, Y. Cheng, X. Liu, and J. Christensen, Directional acoustic antennas based on valley-hall topological insulators, *Adv. Mater.* **30**, 1803229 (2018).
- [24] B.-Z. Xia, S.-J. Zheng, T.-T. Liu, J.-R. Jiao, N. Chen, H.-Q. Dai, D.-J. Yu, and J. Liu, Observation of valleylike edge states of sound at a momentum away from the high-symmetry points, *Phys. Rev. B* **97**, 155124 (2018).
- [25] C. He, S.-Y. Yu, H. Ge, H. Wang, Y. Tian, H. Zhang, X.-C. Sun, Y. B. Chen, J. Zhou, M.-H. Lu, and Y.-F. Chen, Three-dimensional topological acoustic crystals with pseudospin-valley coupled saddle surface states, *Nat. Commun.* **9**, 4555 (2018).
- [26] Y. Shen, C. Qiu, X. Cai, L. Ye, J. Lu, M. Ke, and Z. Liu, Valley-projected edge modes observed in underwater sonic crystals, *Appl. Phys. Lett.* **114**, 023501 (2019).
- [27] X. Han, Y.-G. Peng, L. Li, Y. Hu, C. Mei, D.-G. Zhao, X.-F. Zhu, and X. Wang, Experimental Demonstration of Acoustic Valley Hall Topological Insulators with the Robust Selection of C_3v -Symmetric Scatterers, *Phys. Rev. Appl.* **12**, 014046 (2019).
- [28] X. Liu, Q. Guo, and J. Yang, Tunable acoustic valley edge states in a flow-free resonator system, *Appl. Phys. Lett.* **115**, 074102 (2019).
- [29] H. Dai, T. Chen, J. Jiao, B. Xia, and D. Yu, Topological valley vortex manipulation of microparticles in phononic crystals, *J. Appl. Phys.* **126**, 145101 (2019).
- [30] Z.-G. Geng, Y.-G. Peng, P.-Q. Li, Y.-X. Shen, D.-G. Zhao, and X.-F. Zhu, Mirror-symmetry induced topological valley transport along programmable boundaries in a hexagonal sonic crystal, *J. Phys.: Condens. Matter* **31**, 245403 (2019).
- [31] Z. Zhu, X. Huang, J. Lu, M. Yan, F. Li, W. Deng, and Z. Liu, Negative Refraction and Partition in Acoustic Valley Materials of a Square Lattice, *Phys. Rev. Appl.* **12**, 024007 (2019).
- [32] M. Chen, W. Xu, Y. Liu, M. Zhang, D. Pei, H. Jiang, and Y. Wang, Tunable Dirac cones in two-dimensional acoustic metamaterials with matryoshka structure, *J. Acoust. Soc. Am.* **146**, 767 (2019).
- [33] P. Gao, Z. Zhang, and J. Christensen, Sonic valley-Chern insulators, *Phys. Rev. B* **101**, 020301(R) (2020).
- [34] Z. Tian, C. Shen, J. Li, E. Reit, H. Bachman, J. E. S. Socolar, S. A. Cummer, and T. J. Huang, Dispersion tuning and route reconfiguration of acoustic waves in valley topological phononic crystals, *Nat. Commun.* **11**, 762 (2020).
- [35] M. Wang, W. Zhou, L. Bi, C. Qiu, M. Ke, and Z. Liu, Valley-locked waveguide transport in acoustic heterostructures, *Nat. Commun.* **11**, 3000 (2020).
- [36] X. Han, L. Li, Y. Hu, L. Ling, Z.-G. Geng, Y.-G. Peng, D.-G. Zhao, X.-F. Zhu, and X. Wang, Valleylike Edge States in Chiral Phononic Crystals with Dirac Degeneracies beyond High-Symmetry Points and Boundaries of Brillouin Zones, *Phys. Rev. Appl.* **14**, 024091 (2020).
- [37] S. H. Mousavi, A. B. Khanikaev, and Z. Wang, Topologically protected elastic waves in phononic metamaterials, *Nat. Commun.* **6**, 8682 (2015).
- [38] R. K. Pal and M. Ruzzene, Edge waves in plates with resonators: An elastic analogue of the quantum valley-hall effect, *New J. Phys.* **19**, 025001 (2017).
- [39] J. Vila, R. K. Pal, and M. Ruzzene, Observation of topological valley modes in an elastic hexagonal lattice, *Phys. Rev. B* **96**, 134307 (2017).

- [40] H. Zhu, T.-W. Liu, and F. Semperlotti, Design and experimental observation of valley-hall edge states in diatomic-graphene-like elastic waveguides, *Phys. Rev. B* **97**, 174301 (2018).
- [41] M. Yan, J. Lu, F. Li, W. Deng, X. Huang, J. Ma, and Z. Liu, On-chip valley topological materials for elastic wave manipulation, *Nat. Mater.* **17**, 993 (2018).
- [42] J. Wang and J. Mei, Topological valley-chiral edge states of lamb waves in elastic thin plates, *Appl. Phys. Express* **11**, 057302 (2018).
- [43] T.-W. Liu and F. Semperlotti, Tunable Acoustic Valley-Hall Edge States in Reconfigurable Phononic Elastic Waveguides, *Phys. Rev. Appl.* **9**, 014001 (2018).
- [44] T.-W. Liu and F. Semperlotti, Experimental Evidence of Robust Acoustic Valley Hall Edge States in a Nonresonant Topological Elastic Waveguide, *Phys. Rev. Appl.* **11**, 014040 (2019).
- [45] M. Miniaci, R. K. Pal, R. Manna, and M. Ruzzene, Valley-based splitting of topologically protected helical waves in elastic plates, *Phys. Rev. B* **100**, 024304 (2019).
- [46] W. Wang, B. Bonello, B. Djafari-Rouhani, and Y. Pennec, Polarization-dependent and valley-protected lamb waves in asymmetric pillared phononic crystals, *J. Phys. D: Appl. Phys.* **52**, 505302 (2019).
- [47] W. Wang, B. Bonello, B. Djafari-Rouhani, and Y. Pennec, Topological valley, pseudospin, and pseudospin-valley protected edge states in symmetric pillared phononic crystals, *Phys. Rev. B* **100**, 140101(R) (2019).
- [48] Z. Wang, F.-K. Liu, S.-Y. Yu, S.-L. Yan, M.-H. Lu, Y. Jing, and Y.-F. Chen, Guiding robust valley-dependent edge states by surface acoustic waves, *J. Appl. Phys.* **125**, 044502 (2019).
- [49] S. Li, I. Kim, S. Iwamoto, J. Zang, and J. Yang, Valley anisotropy in elastic metamaterials, *Phys. Rev. B* **100**, 195102 (2019).
- [50] Q. Zhang, Y. Chen, K. Zhang, and G. Hu, Dirac degeneracy and elastic topological valley modes induced by local resonant states, *Phys. Rev. B* **101**, 014101 (2020).
- [51] H.-X. Wang, H. Chen, J.-H. Jiang, and G.-Y. Guo, Tunable edge states in reconfigurable photonic crystals, *J. Appl. Phys.* **126**, 193105 (2019).
- [52] J. Lu, C. Qiu, S. Xu, Y. Ye, M. Ke, and Z. Liu, Dirac cones in two-dimensional artificial crystals for classical waves, *Phys. Rev. B* **89**, 134302 (2014).